Electronic Supplementary Material (ESI) for Nanoscale.

Supporting Information

Growth of $MAPbBR_3$ Single Crystal

Chemicals and reagents: Lead(II) Bromide ($PbBr_2$, ≥ 99.99%) and Methylammonium Bromide (MABr, ≥ 99.99%) were purchased from Aldrich and Greatcell Solar Materials. Dichloromethane (DCM, ACS reagent, ≥ 99.9%) and N, N-dimethylformamide (DMF, RPE-ACS reagent) solvents were purchased from Merck and Carlo Erba Reagents companies. All chemicals were used as supplied without further purification.

$MAPbBr_3$ single crystals were prepared using the inverse temperature crystallization method from a dimethylformamide (DMF) solution of the compound. A pure crystalline powder of perovskite was produced by antisolvent method starting from a 1.0 M solution of the hybrid perovskite (40 mL) prepared by dissolving the two precursors $PbBr_2$ and methylammonium bromide in DMF in 1:1 molar ratio. Precipitation of the solute was achieved by fast addition of dichloromethane (60 mL). The mixture was stirred for about one hour before recovering the product by filtration. The precipitate was ground, dried and characterized by X-ray powder diffraction to confirm the purity and crystallinity nature of the material (Rigaku MiniFlex 600 diffractometer).

A solution of $MAPbBr_3$ in DMF at about 1.2 molar concentration was prepared by dissolving 11.5 g of the pure perovskite powder in 20 mL of the solvent. The solution was kept under stirring for about two hours at room temperature and then poured into a clean 100 mL beaker that was placed in a jacketed crystallizer connected to a heating thermostat. The crystals were grown by temperature rising in the range of 50–88° C in according to a defined growth temperature program (2140 min, increasing temperature steps with variable ramp rate between 0.250°/h and 15.0°/h). The crystals were quickly recovered from the hot solution and dried at air.

Single crystal X-ray diffraction analysis

A large (0.9 x 1.9 x 2.4 mm) crystal of $MAPbBr_3$ was grown from DMF by the inverse temperature crystallization method as described in the previous section. An X-ray quality sample was cut from an edge of the bulk crystal using a stainless steel microblade and accurately polished in a drop of inert perfluorinated oil. The specimen was mounted on top of a glass capillary fiber with a drop of the same oil (Figure S1).

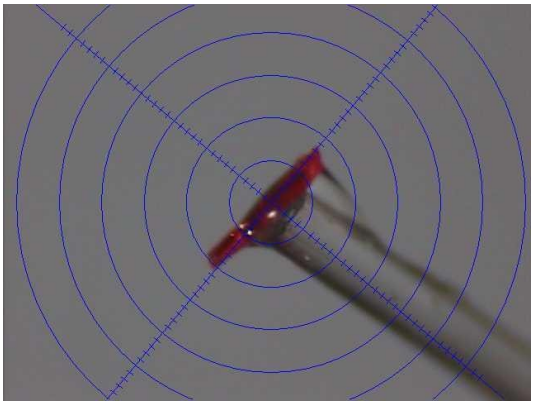

Figure S1. Specimen employed for the X-ray diffraction experiments. A division on the graduate scale corresponds to 25 μm. The dimensions of the crystals are ≈ 0.450 x 0.100 x 0.075 mm.

The X-ray data collection was carried out at room temperature (≈ 300 K) on a Bruker AXS Smart Apex three-circle diffractometer equipped with a CCD detector. A normal focus sealed tube X-ray source with a nominal power of 50 kV x 30 mA was employed to produce a graphite-monochromated Mo Kα beam, with average λ = 0.71073 Å.

A high redundant, 100 % complete full sphere of diffraction effects was recorded using multiple ω–scan strategies at variable scan speed (0.025 or 0.0075 deg·s^{-1}). We obtained a total of 3164 measured reflections, up to a maximum sinϑ/λ of 0.71 $Å^{-1}$, corresponding to a resolution of 0.704 Å. Reciprocal space integration was carried out with SAINT-plus (© Bruker AXS Inc., Madison, Wisconsin, USA, 2012). Due to the large absorption coefficient of this material at the Mo Kα wavelength (μ = 34.716 mm^{-1}), the recorded intensities were carefully corrected for X-ray absorption through the evaluation of an anisotropic multipole absorption surface, with the least-squares method implemented in SADABS (© Bruker AXS Inc., Madison, Wisconsin, USA, 2001). The final dataset consists of 91 symmetry-independent reflections with an internal agreement factor of R_{int} = 0.0245.

The primary atom sites, that is, those of Pb and Br ions, were resolved by alternating modifications of trial structure factor phases in direct and reciprocal space with the charge flipping algorithm[1], while the real space location of the organic CH_3-NH_4^+ (methylammonium, MA^+) cation was

determined from the corresponding difference Fourier maps. The structural model was refined by the least-squares algorithm as implemented in shelxl[2]. The same strategy suggested by Elbaz *et al.*[3] was exploited to deal with the intrinsic disorder of the organic cation (see also the discussion below). Secondary extinction was included in the model, resulting in an estimated extinction coefficient of 0.033(2). The final model refined to agreement factors as low as R1(F) = 0.0106, wR(F^2) = 0.0305 over the whole dataset, with a goodness-of-fit of 1.271. These correspond to maximum Fourier residuals $\Delta\rho_{MAX/MIN}$ = +0.69/ –0.49 e/Å^3 in the unit cell space.

Full crystallographic information, including the last least squares input and the experimental structure factor, is deposited in a crystallographic information file (.cif) as supplementary data to the present work.

This X-ray structure determination was carried out with a twofold purpose. First, to determine the crystallographic quality of the synthesized $MAPbBr_3$ crystals and, second, to provide an up-to-date description of the structure at the molecular level. Despite cutting of the original bulk crystal, the fragment here examined has a very good quality, with almost negligible stress–induced features in the reciprocal lattice, as testified by the absence of significant diffuse scattering features in the reconstructed precession images (Figure S2). Cutting does not degrade the overall quality of the material, at least from the crystallographic viewpoint.

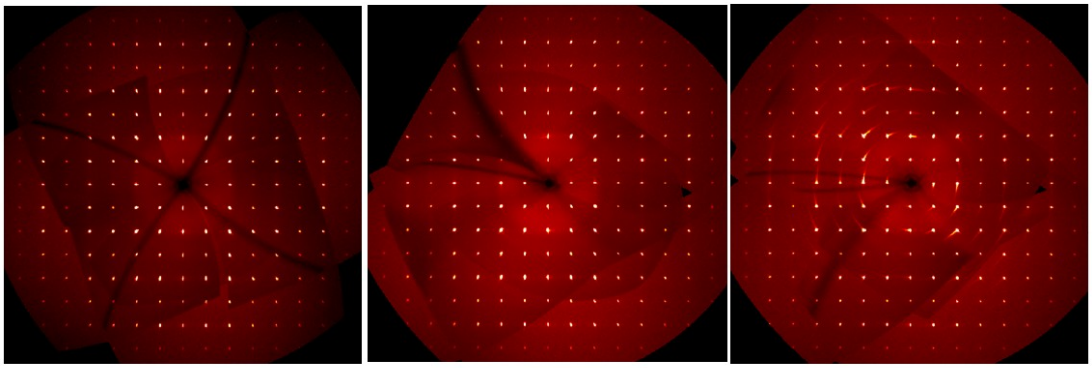

Figure S2. Reconstructed precession images of the diffraction output from the crystal in the equatorial plane of the reciprocal lattice, as viewed down the reciprocal edges *a** (left), *b** (centre), *c** (right).

We obtained the cubic centric apolar $Pm\underline{3}m$ *phase*. The unit cell was estimated from 2692 intense reflections among 6.8 and 59.8 deg in 2ϑ. The refined cell edge is *a* = 5.9175(3) Å, corresponding to a volume V = 207.21(3) Å^3, in very good agreement with recent Literature estimates.[3,4,5] The material has the expected ABX_3 perovskite structure with A = methylammonium (MA^+), B = Pb^{2+} and bromide Br^- species as counterions (Figure S3). Thus, each lead cation has 6 Br^- as next neighbours at ½ of the lattice parameter, and 8 MA^+ at ½ of the cube body diagonal.

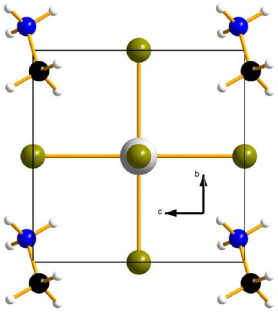

Figure S3. Structural model for the cubic unit cell of the $MAPbBr_3$ perovskite single crystal, seen along the *a* axis. The MA^+ cations sitting on the vertices are actually rotationally disordered. The colours have the following meaning: grey, Pb^{2+}; dark green, Br^-; black, C; blue, N; white, H. Direct Pb-Br interactions are highlighted as yellow lines.

MA^+ cations have their centre of gravity very close (possibly coincident) with the (0,0,0) Wyckoff 1*a* special position, but individual CH_3 and NH_3 groups occupy general 48*n* positions. This implies that each ion is rotationally disordered through 48 symmetry–equivalent orientations. According with recent experimental evidence, this intrinsic rotational disorder bears significant dynamic contributions.[6] In fact, lowering T triggers partial ordering of the MA^+ ions in these perovskite structures,[7] breaking the $m\bar{3}m$isotropy of the crystal field and thus possibly causing a distortion to less symmetric structures that could develop ferroelectric and antiferroelectric domains.[8]

The macroscale self-assembly, 3D packing, crystalline quality ed emission of the $MAPbBr_3$ single crystal are characterized directly on the final device by confocal z-stack microscopy, in transmission mode and shown in Figure S4.

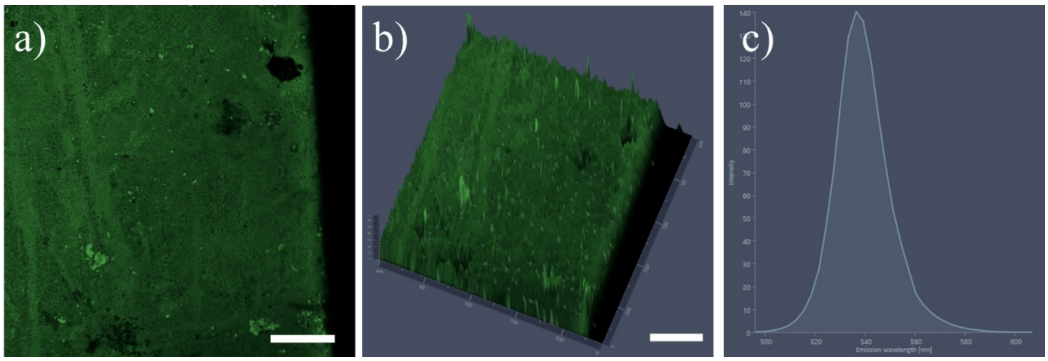

Figure S4. Confocal characterization of the MaPbBr3 specimen employed. a) 2D confocal image obtained with a 405 nm-laser excitation and collecting the spectrum over the emission range; b) 3D z-stack reconstruction of the same crystal obtained by the confocal acquisition over the crystal's thickness Spatially Resolved-PL of an area of the crystal. Scale bars: 50 µm.

Simulation of the energy deposited in the crystal by a 300 MeV electron

Using the GEANT4 simulation framework we simulated the passage of 300 MeV energy electrons (as delivered by the BTF beamline) in the detector and derived the deposited energy. The derived distribution is compared to the one obtained simulating muons/protons with momentum p/mc ≈ 3 corresponding to the minimum of the ionisation curve described by the Bethe-Block formula. Figure S5 shows the different distribution and mean energy deposited in the case of electrons from the BTF and minimum ionising muons/protons. The mean deposited energies differ by about 15%. As electrons with 300 MeV energy also lose energy through Bremsstrahlung, i.e. the emission of photons from electrons deflected by the Coulomb field of a nucleus, we disentangled the mere contribution of the energy deposition by ionization for 300 MeV electrons: the Bremsstrahlung contribution in the 1.4 mm thick perovskite crystal is estimated to be negligible.

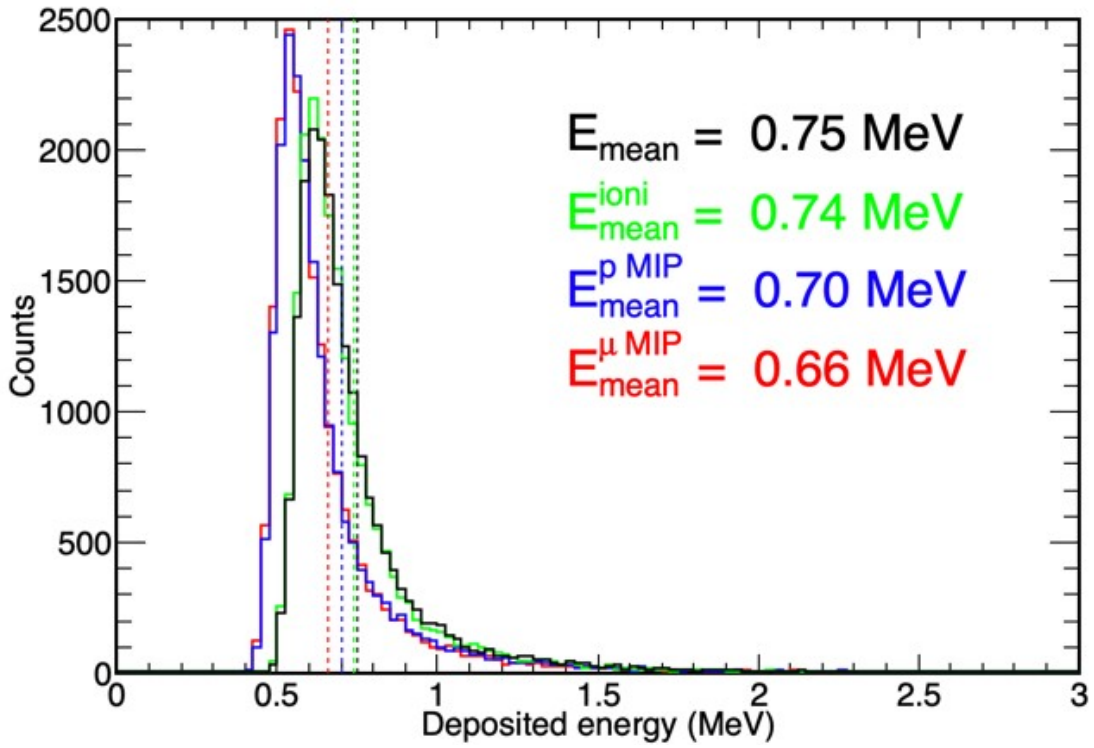

Figure S5. Simulated energy deposited in the SC by 300 MeV electrons in black, minimum ionizing muons in red, minimum ionising protons in blue and by 300 MeV electrons that can only interact by ionization in green. Total simulated events are 50k.

Electrical characteristics

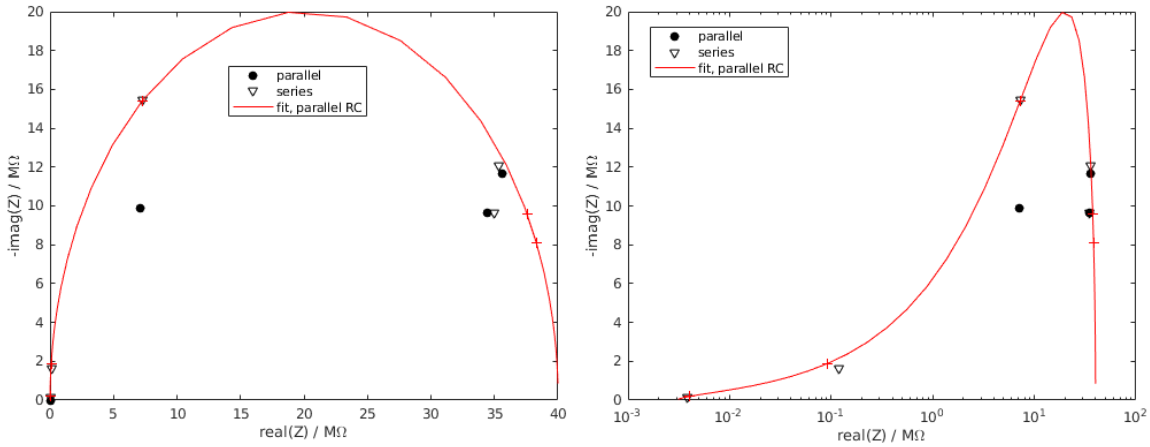

Figure S6. Complex impedance measured at different frequencies (100, 120, 10^3, 10^4, 10^5 Hz) using an RLC meter (black symbols), and fit using a parallel RC circuit with additional series resistance (red curve, crosses at measurement frequencies). The measured impedance has been extracted both for series and parallel configuration. The logarithmic plot on the right shows the fit at high frequencies. We obtained R_s = 3100 Ω, R_p = 38 MΩ, C_p = 9.84 pF.

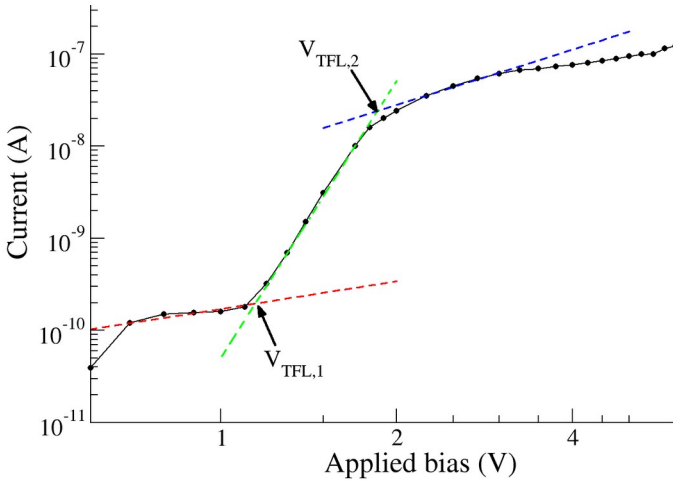

Figure S7. Dark JV characteristic of the device in log-log scale, used for space-charge limited current analysis. The measurement has been performed in quasi-static regime. According to Ref. [9], we used $V_{TFL,2}$ = 1.85 V to extract the trap density, as this appears to be more reliable.

Electron multiplicities

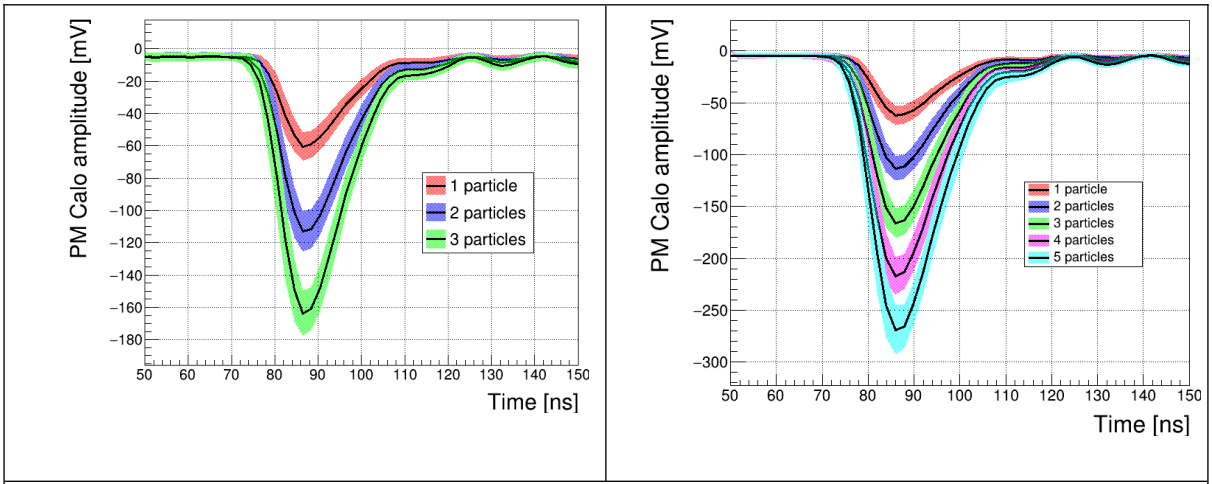

Figure S8. Averaged calorimeter signal waveforms with 1 to 3/5 particles per event for the sample with <μ> = 1.4 (left) and 5 (right). The photomultplier bias voltage has been set to 1.2 kV. Time is the same as for the Fig. 2 on a different scale. Bands represent the R.M.S. of the observed values in the subset with fixed number of particles. The calorimeter signal is much faster and stable and allow good separation between multiplicity.

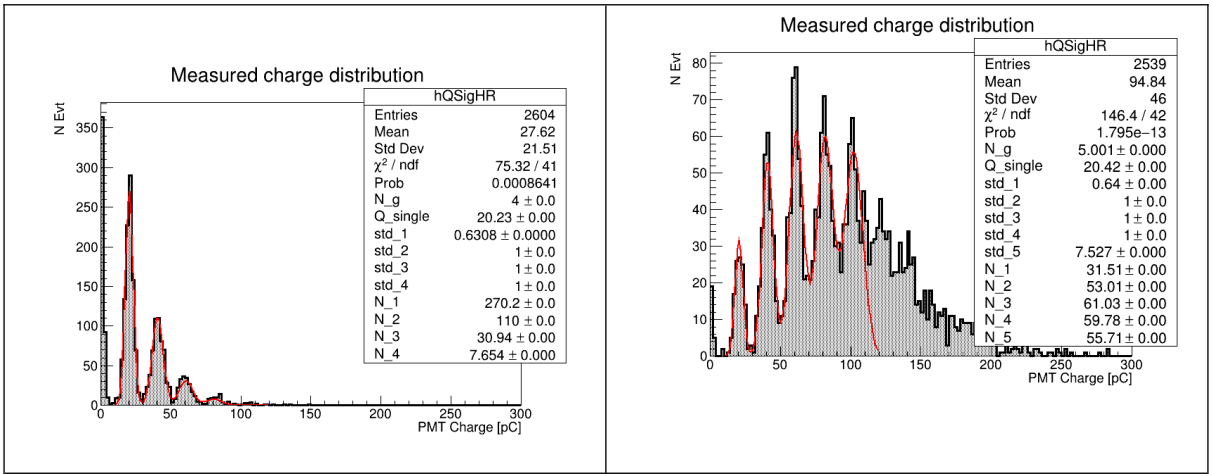

Figure S9. Collected charge distribution from the calorimeter photo-multiplier for the run with mean electron multiplicity 1.4 (left) and 5 (right) used in the text [Fig.2 and Table 1]. The pedestals has been subtracted. The fit function is written below and represent a superposition of Gaussian having a common scaling for mean value and for width. The free variables in the fit are the charge and the width of the single particle peak and the normalization of each peak, that in the chosen parametrization express the height of the peak for the corresponding multiplicity. This parametrization imply automatically the

general assumption that signal associated with many electrons are simply propoportional to the single electron response trough the number of impinging particles.
Multiplicity fit function:

$$f(Q) = \sum_i N_i exp((Q - Q_i)^2/2\sigma_i^2)\Big|_{Q_i = iQ_1; \sigma_i = \alpha\sqrt{Q_i}}$$

The fit results for the single particle parameters are compatibles between the two samples and shows a clear linearity of the response of the calorimeter used for event selection.
Fit reults are shown in the plots. In both cases Q_1~20 pC and α ~0.64.

Dedicated cuts allowed to split the data for each sample in subsets having well defined particle multiplicity. From the right plot it is clearly visible that it is not possible to fully separate events with multiplicity higher than five electrons per shot because of the resolution.

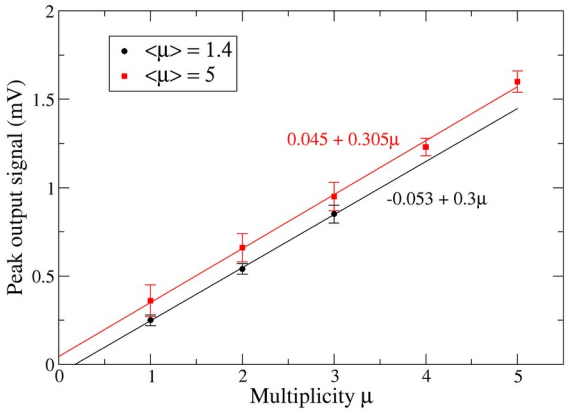

Figure S10. Perovskite peak output signal as a function of multiplicity, at low mean beam multiplicities. The observed values for the two samples are in good agreement within the experimental errors.

Fitting of the output signal

The output signal has been fitted by a triple exponential function. Two of the exponentials are related to the amplifier circuit's impulse response, including the high pass filter due to the ac coupling at the output, while the third exponential assumes an exponentially decaying current pulse at the amplifier input as $i(t)=i_0 \exp\left(\frac{-t}{\tau_D}\right)$. Assuming that the Hecht model can be applied, i.e. that charge transport is due to drift only and the electric field is constant in the device, then τ_D can be interpreted as the carrier lifetime. The extracted charge is given by $Q_{extr}=i_0 \cdot \tau_D$.
In Laplace transformed form, the output signal is written as

$$U(s)=\frac{i_0}{s+\tau_D^{-1}} \cdot \frac{R_f}{1+s R_f C_f} \cdot \frac{s C_o}{1+s 2 R_o C_o}$$

Here, R_f and C_f are the feedback elements of the charge amplifier (100 MΩ and 1.4 pF), and C_o = 1 µF is the output coupling capacitor, while $R_o$is the 50 Ω resistance at the output. Note that the time constant of the third term is similar to the one of the charge amplifier, which is why the output signal is distorted and the extracted charge cannot be evaluated by time integration.

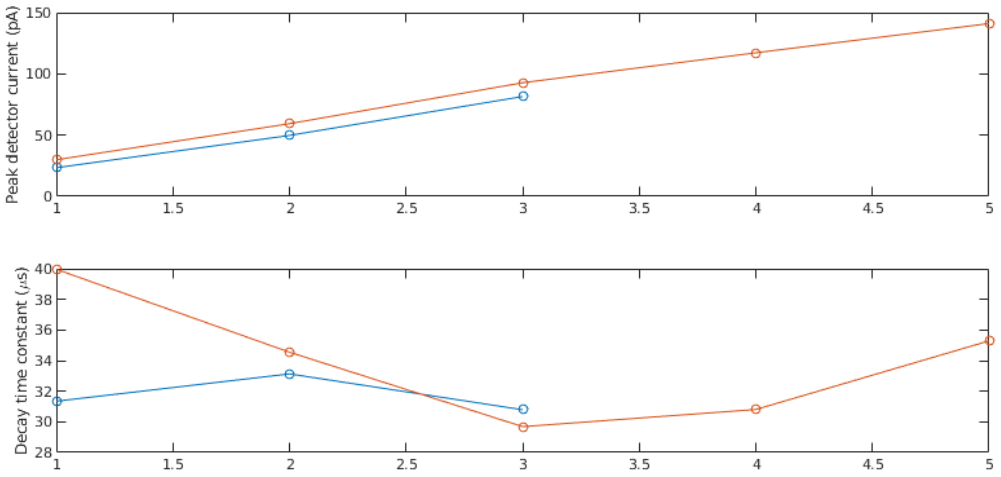

Figure S11. Input signal parameters as a function of multiplicity, for the two low multiplicity cases at 5 V bias. The case of $\langle \mu \rangle = 1.4$ is less affected by noise and gives a consistent lifetime of ~ 32 µs.

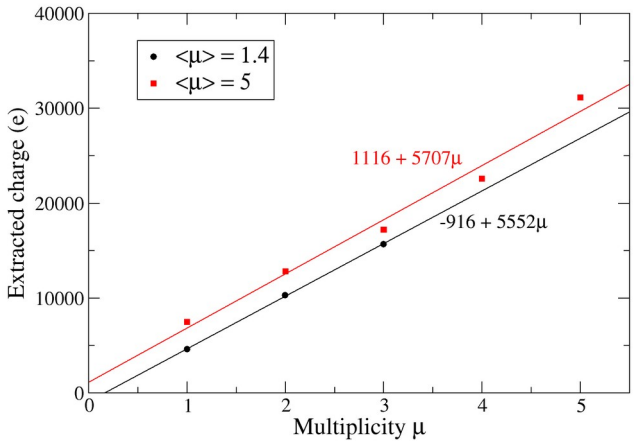

Figure S12. Extracted charge as a function of multiplicity. Roughly 5600 electrons are extracted per incident high energy electron, corresponding to roughly 4.35% extraction efficiency.

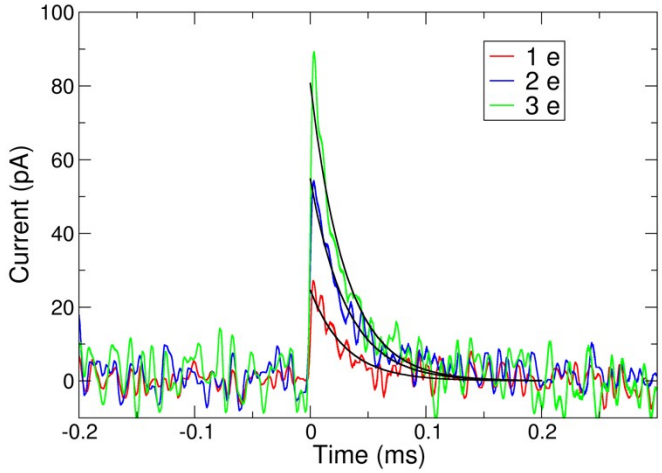

Figure S13. Input signals for the case of $\langle \mu \rangle$=1.4, obtained by filtering and deconvolution with the amplifier's impulse response. The black lines are exponential fits with decay time of 32 μs, confirming the assumption of an exponential current pulse from the detector.

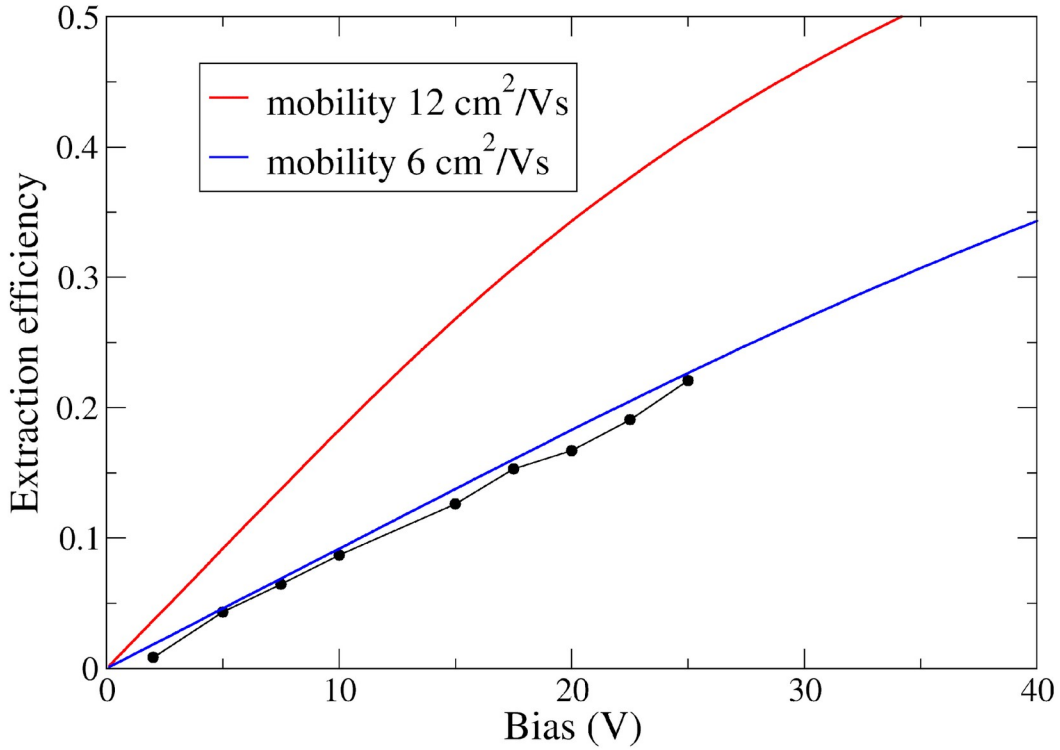

Figure S14. Extraction efficiency at different bias voltages, and comparison with the Hecht model. The data fits well the model when assuming a smaller mobility of 6 cm^2/Vs. Note that the mobility extracted from the dark IV curve may not be very accurate, as it relies on specific model assumptions. Moreover, we expect the minority carriers to be electrons, while the dark IV reflects properties of the holes.

TCAD simulations

We have performed TCAD simulations to qualitatively reproduce the device response, using Synopsys Sentaurus TCAD[10]. We assumed circular symmetry, with a single particle trajectory at the center generating electron-hole pairs according to different numbers of high energy electrons (130000 e-h pairs per incident electron, assuming all to pass in the same location), using the HeavyIon model. The simulation domain was up to a radius of 100 µm. Contacts have been modeled as Schottky contacts with effective barrier of 0.3 eV. Transient simulations at a bias of 5 V for 1-5, 10, 100, 100 and 1000 e^- have been performed, and the current transients recorded. Using a trap density of $5x10^9$ cm^{-3}, we obtain a fair correspondence in the value of $V_{TFL,2}$, with approximately 1.8 V from the simulation versus 1.85 V from the measured characteristic. Clearly, the comparison of the dark JV is only qualitative, although the absolute value of the current at 5 V is in the range of the experimental value, as shown in Figure S14.

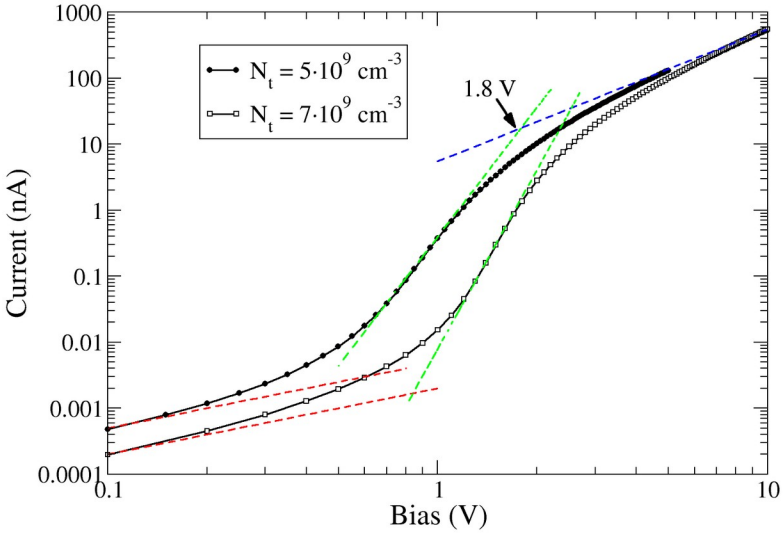

Figure S15. Dark JV simulated for two different trap densities. The dashed lines indicate the slopes in the different regions as in Figure S7.

The simulated transients are similar to the ones extracted from the measured signals. They are substantially exponential, with a decay time of roughly 30 µs, controlled by the SRH lifetime defined in the simulation model. We have used 15 µs for each carrier, which in case of approximately equal carrier densities in fact leads to an effective doubled lifetime, since $R_{SRH} \approx \frac{np}{\tau_n p + \tau_p n} \approx \frac{n}{\tau_n + \tau_p}$. The following Figure shows the signal up to 10^4 electrons per bunch.

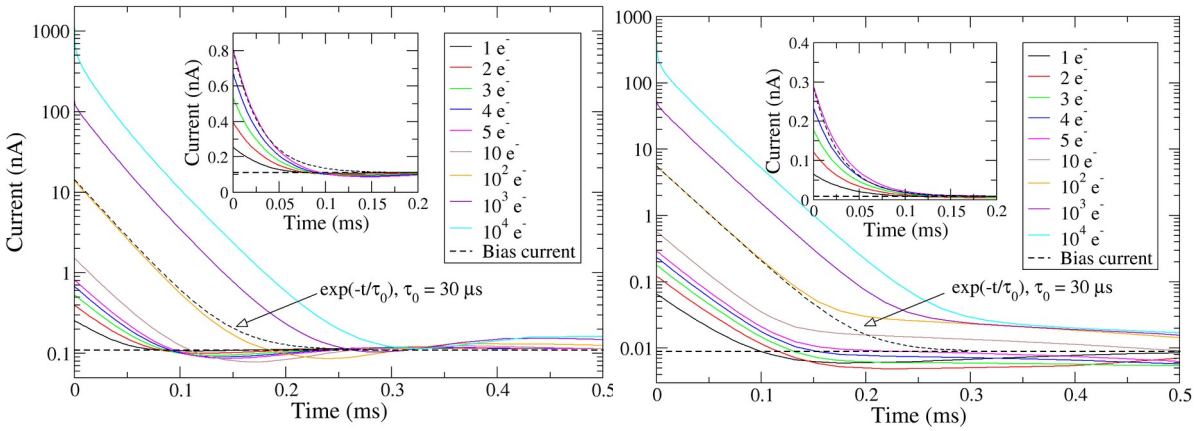

Figure S16. Transients at a bias of 5 V (left) and 2V (right) for different multiplicities. The quiescent bias current of 0.11 nA is comparable to the measured current. The dashed line indicates a single exponential decay for comparison.

The next Figure shows the extracted charge at 5 V and 2 V bias, in comparison with the measured values. The simulation gives a roughly 4 times larger extraction efficiency. However, the linearity is similar, and only at multiplicity above 1000 the slope decreases, which is compatible with the experimental data. The cause is probably increased recombination due to radiative recombination, which in fact becomes dominant during the first few µs. We did not observe evident signs of screening in the simulation results, which is due to the electron and hole densities being relatively small and similar in size throughout the transient.

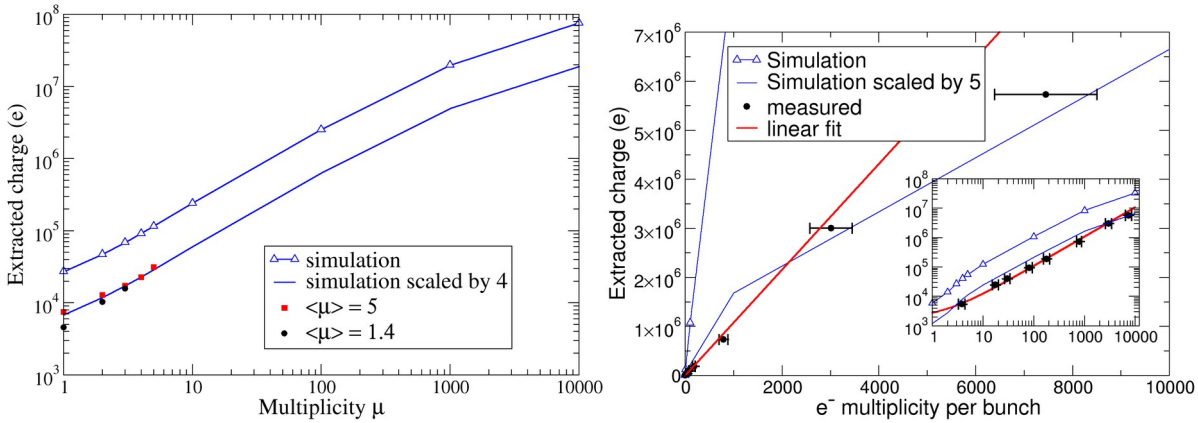

Figure S17. Extracted charge for a bias of 5 V (left) and 2 V (right).

References

[1] G. Oszlányi and A. Süto, *Acta Cryst*. 2004, A**60**, 134-141, DOI: 10.1107/S2052519212051366

[2] G. M. Sheldrick, *Acta Cryst.* 2015, C**71**, 3-8, DOI: 10.1107/S2053229614024218

[3] G. A. Elbaz, D. B. Straus, O. E. Semonin, T. D. Hull, D. W. Paley, P. Kim, J. S. Owen, C. R. Kagan and X. Roy, *Nano Letters* 2017, **17**, 1727–1732 DOI: 10.1021/acs.nanolett.6b05022

[4] Y. Wang, X. Lü, W. Yang, T. Wen, L. Yang, X. Ren, L. Wang, Z. Lin and Y. Zhao*, J. Am. Chem. Soc*. 2015, **137**, 11144–11149, DOI: 10.1021/jacs.5b06346

[5] I. Viola, F. Matteocci, L. De Marco, L. Lo Presti, S. Rizzato, S. Sennato, A. Zizzari, V. Arima, A. De Santis, C. Rovelli, S. Morganti, M. Auf der Maur and M. Testa, *Adv. Mater. Technol.* 2023, **8**, 2300023 DOI: 10.1002/admt.202300023

[6] R. E. Wasylishen, O. Knop and J. B. Macdonald, *Solid State Commun*. 1985, **56** (7), 581– 582, DOI: 10.1016/0038-1098(85)90959-7 34

[7] N. P. Gallop, O.Selig, G. Giubertoni, H. J. Bakker, Y. L. A. Rezus, J. M. Frost, T. L. C. Jansen, R. Lovrincic and A. A. Bakulin *J. Phys. Chem. Lett.* 2018, **9**, 20, 5987–5997, DOI: 10.1021/acs.jpclett.8b02227

[8] A. M. A. Leguy, J. M. Frost, A. P. McMahon, V. G. Sakai, W. Kockelmann, C. Law, X. Li, F. Foglia, A. Walsh and B. C. O'Regan, *Nat. Commun*. 2015, **6**(1), 7124, DOI: 10.1038/ncomms8124

[9] V. M. Le Corre, E. A. Duijnstee, O. El Tambouli, J. M. Ball, H. J. Snaith, J. Lim and L. J. A. Koster, *ACS Energy Letters*, 2021, 6, 1087–1094, DOI: 10.1021/acsenergylett.0c02599

[10] Synopsys Sentaurus Device, Version U-2022.12